

Reference Design and Simulation Framework of a Multi-Megawatt Airborne Wind Energy System

Dylan Eijkelhof¹, Sebastian Rapp¹, Urban Fasel², Mac Gaunaa³ and Roland Schmehl¹

¹Faculty of Aerospace Engineering, Delft University of Technology, Kluyverweg 1, 2629 HS Delft, The Netherlands

²Laboratory of Composite Materials and Adaptive Structures, Swiss Federal Institute of Technology, Leonhardstrasse 21, 8092 Zürich, Switzerland.

³DTU Wind Energy, Technical University of Denmark, Frederiksborgvej 299, 4000 Roskilde, Denmark.

E-mail: r.schmehl@tudelft.nl

Abstract. In this paper, we present the design and computational model of a representative multi-megawatt airborne wind energy (AWE) system, together with a simulation framework that accounts for the flight dynamics of the fixed-wing aircraft and the sagging of the tether, combining this with flight control and optimisation strategies to derive the power curve of the system. The computational model is based on a point mass approximation of the aircraft, a discretisation of the tether by five elastic segments and a rotational degree of freedom of the winch. The aircraft has a wing surface area of 150 m² and is operated in pumping cycles, alternating between crosswind flight manoeuvres during reel out of the tether, and rapid decent towards the ground station during reel in. To maximise the net cycle power, we keep the design parameters of the aircraft constant, while tuning the operational and controller parameters for different wind speeds and given constraints. We find that the presented design can generate a net cycle power of up to 3.8 megawatts.

1. Introduction

Currently developed AWE systems have reached sizes of up to several hundred kilowatts [10, 20]. Some representative examples are shown in Figure 1 [4, 22]. However, no commercial utility-



Figure 1. Selected AWE systems currently in development: Kitepower, EnerKite, TwingTec, Ampyx Power and Makani Power (from left to right), generating up to 600 kW per single system.

scale product has yet been released to the market [9, 24]. For this next scaling step towards



megawatts, computational tools for the simulation of the entire AWE system covering all relevant physics will be indispensable, not only for saving costs but also for accelerating the pace of technology development. Reference models for the major conversion concepts will be important for benchmarking and cross validating these simulation toolchains. The value of such reference models is best demonstrated by the 5 MW reference wind turbine for offshore system development, which was proposed by the National Renewable Energy Laboratory (NREL) [11], rapidly adopted by the wind energy research community and in consequence contributed majorly to the knowledge base on large-scale wind turbines.

A comparable, publicly available reference model of a megawatt-scale AWE system does not exist at present. Because of the availability of measurement data from prototype testing, the situation is different at smaller scale. For example, a dynamic model of the Ampyx Power AP-2 (see Figure 1, second photo from right) was proposed as a reference model and used for an optimisation study in [17]. The aircraft, which was first flown in 2009, has a wing span of 5.5 m, is operated in pumping cycles generating a rated net power of 10 kW [15, 13]. For the larger AP-3, a computational study of the 3D flow field was presented in [23]. The characteristic twin fuselage aircraft is currently being manufactured, has a wing span of 12 m and will generate a net power of 200 kW [13]. The largest AWE system to date, the Makani M600 (see Figure 1, first photo from right) has been investigated in computational studies that focused on the aeroelastic behaviour of the main wing and the aerodynamics of the entire aircraft but did not cover the energy production of the system [25, 3, 18].

With the present work, we build on a previously developed reference design of a utility-scale fixed-wing AWE system [6]. This design was inspired by the Ampyx Power AP-3/4 and was sufficiently detailed to create an aeroelastic model of the main wing and use this to study the flight behaviour and deformation of a wing performing circular flight manoeuvres [6]. The reduced order model of the aeroelastic wing was developed earlier and used for a small-scale tethered aircraft [8]. For the present paper, we deactivated the aeroelastic model and implemented a flight controller for operating the wing in pumping cycles, performing figure-of-eight flight manoeuvres during reel out of the tether and diving towards the ground station during reel in. This specific flight controller was used previously for the simulation of a small-scale tethered aircraft [21]. The simulation framework is implemented in MATLAB Simulink and the numerical solver combines a three degrees of freedom (DOF) model of the aircraft with a tether model using five elastic segments and a rotational DOF model of the winch [7]. The iterative solver uses a set of pre-calculated aerodynamic force lookup tables.

The paper is structured as follows. In Section 2, we outline the design of the reference system. In Section 3 we introduce the point mass model of the tethered aircraft and combine this in Section 4 with a simple model for the vertical profile of the wind speed. In Section 5 we describe the control system to operate the dynamic model in pumping cycles and in Section 6 the optimisation technique to maximise the power output by adjusting the operational and controller parameters. After discussing the results in Section 7 we conclude the paper in Section 8.

2. Rigid-wing kite design

The tethered aircraft design is shown in this section. As a more detailed description can be found in [6], only the most important planform parameters and design choices are presented here. A visual representation of the wing and its main dimensions are shown in Figure 2. Table 1 gives brief summary of planform parameters of the main wing, fuselages, tail and tether.

2.1. Airframe layout

The conceptual design of the AP-4 was taken as a starting point for the design of this reference system [12, 1]. As not much was published yet for the AP-4 aircraft at the time of creating this design, the published planform type for the AP-3 aircraft is taken instead [14] assuming the

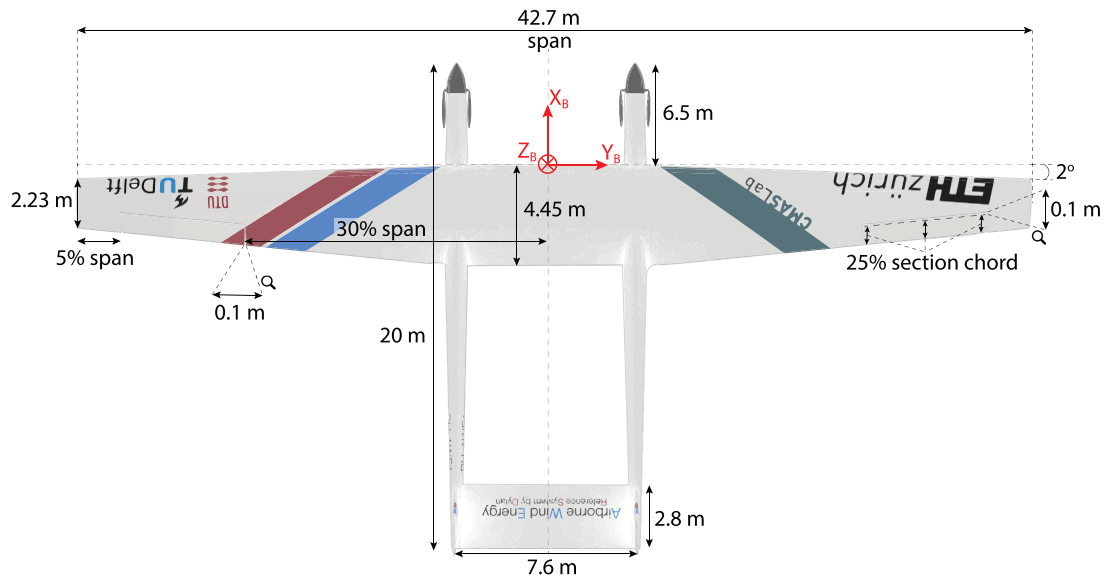


Figure 2. Wing planform (top view).

AP-4 will be an up-scaled version of the AP-3 aircraft. Therefore, a twin-fuselage configuration is chosen, which contributes to the benefit of having appropriate tether clearance during take-off and landing [5]. This configuration also allows the necessary propulsion power during take-off to be divided over two propellers, one at the front of each fuselage. Not only the fuselage layout but also the tether configuration is assumed the same as the AP-3 aircraft. The tether is connected under the main wing as close to the centre of gravity as possible. Multiple tethers can provide a beneficial amount of redundancy and safety, however it will increase aerodynamic drag and thus decreases the power. Combining this with the additional material and maintenance costs, the price of energy will increase which is a big disadvantage on the economic market [13]. The centre of gravity is measured from the leading edge of the main wing. The wing span is sized with a varying root and tip chord in order to achieve a 150 m^2 surface area and an aspect ratio of 12. The wing span is continuously compared to the wing span of the AP-4 aircraft as a sanity check during the sizing process. The front and back spar position and total number of ribs were determined by initial optimisations to maximise the wing load factor (buckling load divided by weight). The ailerons are sized following the design approach of [2]. The ailerons are then extended from 60 to 90% of the halfspan. The 10% left at the wing tip is not used for the aileron as the vortex flows present here provide little control effectiveness. Historical guidelines show that for 30% of the span, typically the aileron chord takes up about 25% of the wing section chord. The sweep is taken rather small.

During the design process done in [6] the focus has been mainly on designing the internal structure of the main wing and setting up a simulation framework that could potentially optimise a system for a desired objective, the design of the two tail sections are solely dependent on rough estimations. The horizontal and vertical stabiliser are initially sized by determining the ratios between tail section and main wing used for the AP-3 design by Ampyx Power. These ratios, however, were not provided by Ampyx Power. This resulted in the dimensions presented in Table 1. The stability of the aircraft is monitored closely throughout the simulations to make sure the aircraft can perform its pumping cycle and small corrections were made accordingly.

Table 1. General planform parameters of the wing, tail, fuselage and tether.

Parameter	Units	Value
Centre of gravity	[m,m,m]	-1.67, 0, 0.229
Total aircraft mass	[kg]	6885.2
<i>Wing:</i>		
Span	[m]	42.7
Chord _{root}	[m]	4.45
Chord _{tip}	[m]	2.23
LE sweep	[°]	2
Aspect ratio	[-]	12.1
Surface area	[m ²]	150.3
Airfoil _{root}	[-]	RevE _{HC} [6]
Airfoil _{tip}	[-]	RevE _{HC} [6]
Front spar	[% c _{local}]	33.3
Back spar	[% c _{local}]	43.4
Aileron _{root-innerrib}	[% b _{1/2}]	60
Aileron _{root-outerrib}	[% b _{1/2}]	90
Aileron _{LE-spar}	[% c _{local}]	75
Total number of ribs	[-]	50
Twist _{root} (Positive Y _B rotation)	[°]	5
Twist _{tip} (Positive Y _B rotation)	[°]	0
<i>Horizontal tail/Elevator:</i>		
Span	[m]	7.6
Chord	[m]	2.8
Airfoil	[-]	NACA 0012
<i>Vertical tail:</i>		
Span	[m]	3
Chord	[m]	2.8
Airfoil	[-]	NACA 0012
<i>Fuselages:</i>		
Length	[m]	20
Radius	[m]	0.6
X _{Nose-LE_{wing}}	[m]	6.5
Y _{Root-Fuselage}	[m]	3.8
<i>Tether:</i>		
Diameter	[m]	0.0297
Minimum length($V_{w,ground} = 12 \text{ m s}^{-1}$)	[m]	526.3
Maximum length($V_{w,ground} = 12 \text{ m s}^{-1}$)	[m]	1434

2.2. Aerodynamic properties

The aircraft dynamics are modelled by a 3DOF point-mass, therefore it is chosen to use only a simplified aerodynamic model with pre-computed static aerodynamic coefficients. Using the FSI algorithm described in [8], the 3D wing is analysed between the minimum and maximum angles of attack. These angles are computed as described in [6]. The calculated lift and drag coefficients are shown in Figure 3, measuring the angle of attack between the relative flow velocity at the aircraft, also denoted as apparent wind velocity, and the x_B -axis of the body-fixed reference frame of the aircraft, which is aligned with the fuselages. The angle of attack is kept with the linear lift region as stall is not taken into account.

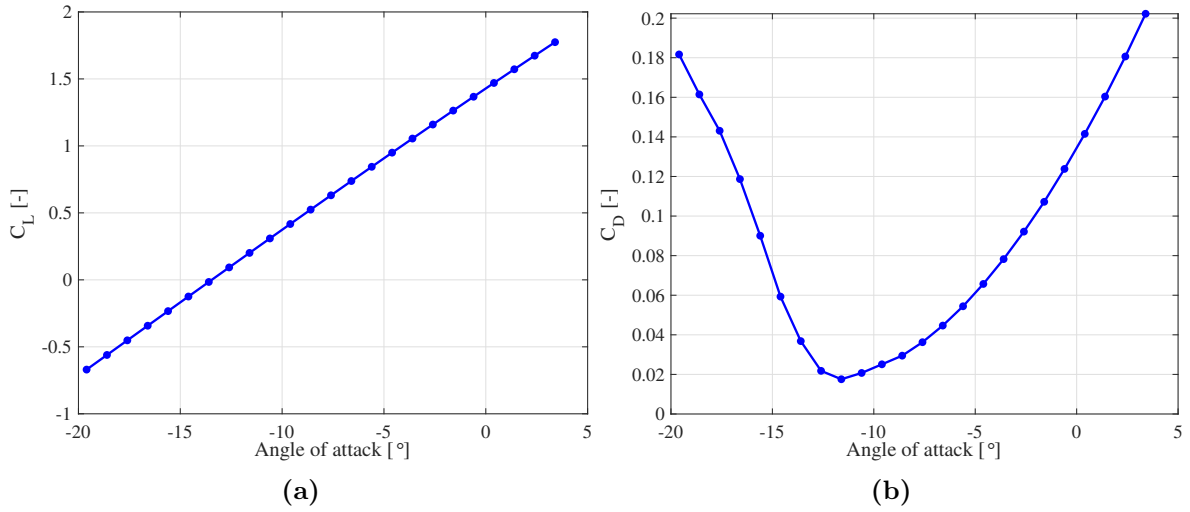


Figure 3. (a) Lift coefficient versus angle of attack. (b) Drag coefficient versus angle of attack, both assessed at $V_a=60 \text{ m s}^{-1}$ and zero side-slip.

3. Point-mass aircraft equations of motion with wind

The three degrees of freedom aircraft dynamics in the rotated aerodynamic frame \bar{A} are given by the three aircraft translations in X, Y and Z direction, hence no rotational dynamics. To obtain a representation which is more useful with point-mass dynamics, the vector containing V_a , χ_a , γ_a is used instead and derived as follows assuming a flat, non-rotating earth and O is regarded as an inertial frame:

$$\mathbf{V}_k = \mathbf{V}_a + \mathbf{V}_w \quad (1)$$

$$\frac{d}{dt}(\mathbf{V}_k)_O = \dot{\mathbf{M}}_{O\bar{A}}(\mathbf{V}_a)_{\bar{A}} + \mathbf{M}_{O\bar{A}}(\dot{\mathbf{V}}_a)_{\bar{A}} + (\dot{\mathbf{v}}_w)_O \quad (2)$$

$$\mathbf{F} = m\mathbf{a} \quad (3)$$

Combining Equations (2) and (3) and rewriting leads to the following:

$$\mathbf{M}_{\bar{A}O} \frac{1}{m_a} \sum_i (\mathbf{F}_i)_O = \mathbf{M}_{\bar{A}O} \dot{\mathbf{M}}_{O\bar{A}}(\mathbf{V}_a)_{\bar{A}} + (\dot{\mathbf{V}}_a)_{\bar{A}} + \mathbf{M}_{\bar{A}O}(\dot{\mathbf{v}}_w)_O \quad (4)$$

$$\frac{(\mathbf{F}_{tot})_{\bar{A}}}{m_a} = \begin{pmatrix} 0 \\ \dot{\chi}_a \cos \gamma_a V_a \\ -\dot{\gamma}_a V_a \end{pmatrix}_{\bar{A}} + \begin{pmatrix} \dot{V}_a \\ 0 \\ 0 \end{pmatrix}_{\bar{A}} + \begin{pmatrix} \dot{v}_{w,x} \\ \dot{v}_{w,y} \\ \dot{v}_{w,z} \end{pmatrix}_{\bar{A}} \quad (5)$$

$$\begin{pmatrix} \dot{V}_a \\ \dot{\chi}_a \\ \dot{\gamma}_a \end{pmatrix}_{\bar{A}} = \begin{pmatrix} 1 & 0 & 0 \\ 0 & \frac{1}{V_a \cos \gamma_a} & 0 \\ 0 & 0 & \frac{-1}{V_a} \end{pmatrix}_{\bar{A}} \left[\frac{(\mathbf{F}_{tot})_{\bar{A}}}{m_a} - \begin{pmatrix} \dot{v}_{w,x} \\ \dot{v}_{w,y} \\ \dot{v}_{w,z} \end{pmatrix}_{\bar{A}} \right], \quad (6)$$

where V_a , χ_a , γ_a and m_a represent true airspeed, aerodynamic course angle, path angle and aircraft mass, respectively. $\dot{v}_{w,x,\bar{A}}$, $\dot{v}_{w,y,\bar{A}}$ and $\dot{v}_{w,z,\bar{A}}$ represent the total derivatives of the wind velocity in the \bar{A} frame. The resultant force $(\mathbf{F}_{tot})_{\bar{A}}$ consists of gravitational, aerodynamic and tether force. The position propagation equation is defined by

$$\begin{pmatrix} \dot{\lambda} \\ \dot{\phi} \\ \dot{r} \end{pmatrix} = \begin{pmatrix} \frac{v_{k,y,\tau}}{r \cos \phi} \\ \frac{v_{k,x,\tau}}{r} \\ -v_{k,z,\tau} \end{pmatrix}, \quad (7)$$

where λ , ϕ and r denote the longitude, latitude as well as the altitude in the small earth reference frame with origin at the ground station. $v_{k,x,\tau}$, $v_{k,y,\tau}$ and $v_{k,z,\tau}$ denote the kinematic velocity vector components in the tangential plane frame τ . They can be calculated using the wind velocity and the aerodynamic speed obtained from Eq. (6) as well as the current position of the aircraft:

$$\begin{pmatrix} v_{k,x,\tau} \\ v_{k,y,\tau} \\ v_{k,z,\tau} \end{pmatrix}_W = \mathbf{M}_{\tau W} \left[\begin{pmatrix} v_{w,x,W} \\ 0 \\ 0 \end{pmatrix}_W + \mathbf{M}_{WO} \mathbf{M}_{O\bar{A}} \begin{pmatrix} V_a \\ 0 \\ 0 \end{pmatrix}_{\bar{A}} \right] \quad (8)$$

It is assumed that the wind field is stationary in time and given by $v_{w,x,W}$ which is a function of altitude (wind shear). The transformation matrices $\mathbf{M}_{\tau W}$, \mathbf{M}_{WO} and $\mathbf{M}_{O\bar{A}}$ are defined in [21].

4. Wind field

The increase in wind speed with altitude is one of the reasons why airborne wind energy systems are promising since they can operate at higher altitudes than conventional wind turbines. In order to calculate the different wind speeds, a relation between reference wind speed and altitude is used. Equation (9) shows a logarithmic profile of the wind. The relation is commonly used in calculating the wind speeds in wind energy and based on the specification in [19].

$$v_w(h) = v_{w,6m} \frac{\log(h/z_0)}{\log(h_{6m}/z_0)}, \quad (9)$$

where $v_{w,6m}$ is the measured ground wind speed at reference height h_{6m} . This wind speed is measured at an altitude of 6 m. z_0 is dependent on the terrain type and taken to be 0.046 which represents terminal flight phases, which include takeoff, approach, and landing [19].

5. Control system

In the following a concise description of the utilised control system is given. For a detailed derivation please refer to [21]. Since in this work only a three degree of freedom model is used to model the aircraft dynamics, only the outer loop of the flight controller as well as the winch controller is required. The flight controller needs to guide the aircraft along a defined figure of eight flight path during the traction phase and a straight line path during the retraction phase. During the traction phase the required course and path angle rates $\dot{\chi}_{k,c}$ and $\dot{\gamma}_{k,c}$ are directly calculated based on the optimised path curvature as well as the current relative position of the aircraft with respect to the path. During the retraction phase the position error with respect to the straight retraction path is translated into a desired course and path angle which are then both passed through a second order reference filter to generate, similar to the figure of eight guidance, smooth reference course and path angle rates.

Inverting the path dynamics and setting the course and flight path angle rates to $\dot{\chi}_{k,c}$ and $\dot{\gamma}_{k,c}$ allows to calculate the required bank angle, $\mu_{a,c}$ and angle of attack, $\alpha_{a,c}$ to generate the necessary manoeuvre forces to follow the path. Usually these reference angles are then tracked by the inner loop which in this work is not required due to the point mass assumption.

To deal with the response delay introduced by the inner loop between commanded $\mu_{a,c}$, $\alpha_{a,c}$ and actual μ_a , α_a imposed on the aircraft, a second-order reference model is used to form a more closely representation of the 6 degree of freedom dynamics. This model includes an amplitude, rate and bandwidth limitation and is defined as follows

$$\begin{pmatrix} \ddot{\mu}_a \\ \ddot{\alpha}_a \end{pmatrix} = -2\zeta_0\omega_0 \begin{pmatrix} \dot{\mu}_a \\ \dot{\alpha}_a \end{pmatrix} - \omega_0^2 \begin{pmatrix} \mu_a \\ \alpha_a \end{pmatrix} + \omega_0^2 \begin{pmatrix} \mu_{a,c} \\ \alpha_{a,c} \end{pmatrix}, \quad (10)$$

and illustrated in Figure 4.

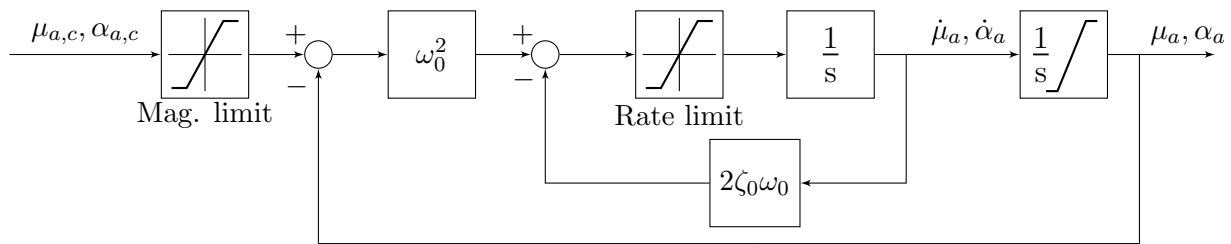


Figure 4. Second-order reference model to track commanded $\mu_{a,c}$, $\alpha_{a,c}$.

The winch controller is slightly simplified compared to the controller in [21]. Instead of calculating a reference torque with a feed forward control structure, the torque command is generated by a simple PI controller where the input is given by the difference between the measured and the commanded tether force. Although this leads to less accurate force tracking, the PI controller yields a more robust performance if winch acceleration limits are taken into account.

6. Optimisation parameters and objective function

The parameters shown in Table 2 are varied by the optimiser in search for maximum average power output. We use the Covariance Matrix Adaptation Evolution Strategy (CMA-ES) optimisation method. The list of parameters is kept short to have a relatively low computational effort. However, the framework is capable of including additional system parameters in the future. The roundness a and width b parameters define the geometry of the figure-of-eight manoeuvre. Figure 5 shows the effect of changing these parameters.

Table 2. Operational and controller parameters that are varied to maximise the power output.

Flight path	Tether force	Controller
Figure-of-eight roundness a	Traction force set point	K_p winch
Figure-of-eight width b	Retraction force set point	K_i winch
Elevation angle		Transition elevation angle
Minimum tether length		Initial path elevation angle
Maximum tether length		$K_{p,\chi}$ traction
		$K_{p,\gamma}$ traction
		$K_{p,\chi}$ retraction
		$K_{p,\gamma}$ retraction
		$K_{i,\chi}$ retraction
		$K_{i,\gamma}$ retraction
		ω_{0,μ_a}
		ω_{0,α_a}
		$\omega_{0,\chi}$ retraction
		$\omega_{0,\gamma}$ retraction

The optimiser follows a specific objective. Several penalties are applied in order to steer the evolution of variables into the desired direction. Penalties are applied for:

- Exceeding the maximum angle of attack (α_a)
- Exceeding the maximum sideslip angle (β)
- Flying too far from the desired trajectory,

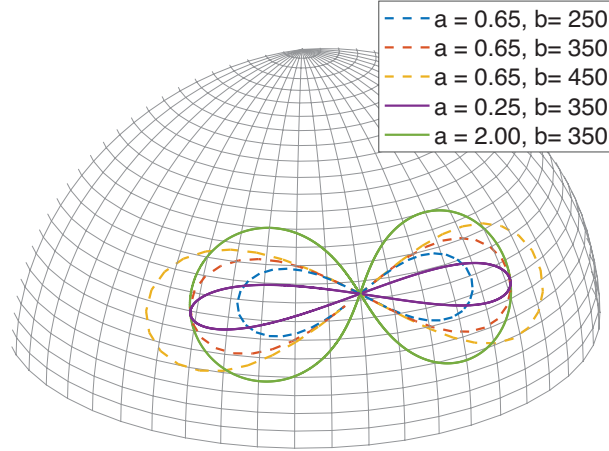


Figure 5. Effect of different roundness a and width b parameters on the tracked flight path.

- Distance to the glide slope during retraction (ϵ_γ)
- Cross-track error (ϵ_c)
- Violating the maximum allowable tether force (F_t)
- Having a too high maximum cycle airspeed (V_a)
- Aggressiveness of the winch in terms of accelerations (a_{winch})

The sum of these penalties are then added to the average produced power (P_{avg}). The cost function (C) is given by Equation (11) and applies only to logged signals from a converged pumping cycle coming from a simulation during the optimisation process. The minus sign is due to the fact that the optimisation framework is designed to minimise its objective.

$$C = p(\epsilon_{\gamma-xy}, \epsilon_{\gamma-z}, \epsilon_c) + p_\beta + p_{\alpha_a} + p_{F_t} + p_{V_a} + p_{W_{Acc}} - P_{avg} \quad (11)$$

with

$$\begin{aligned} p(\epsilon_{\gamma-xy}, \epsilon_{\gamma-z}, \epsilon_c) &= 10^5 \cdot \{ \max(\max(\epsilon_{\gamma-xy})/50\text{m} - 1, 0) \\ &\quad + \max(\max(\epsilon_{\gamma-z})/100\text{m} - 1, 0) \\ &\quad + \max(\max(\epsilon_c)/100\text{m} - 1, 0) \} \\ p_\beta &= 10^5 \cdot \max(\max(\beta)/20^\circ - 1, 0) \\ p_{\alpha_a} &= 10^5 \cdot \max(\max(\alpha_a)/3.4^\circ - 1, 0) \\ p_{F_t} &= 10^6 \cdot \max(\max(F_t)/1.6649 \cdot 10^6\text{N} - 1, 0) \\ p_{V_a} &= 5 \cdot 10^5 \cdot \max(\max(V_a)/90\text{ms}^{-1}, 0) \\ p_{W_{Acc}} &= 10^4 \cdot \text{Var}(a_{winch}) \\ P_{avg} &= \text{Mean}(P) \end{aligned}$$

7. Results

The previously described simulation framework was used to evaluate the performance of the AWE reference system as a point mass. First at a ground wind speed (h_{6m}) of 12 m s^{-1} optimisations are performed to achieve the highest power taking into account the penalties described in Section 6. The power produced during the optimised cycle is shown in Figure 6. The theoretical maximum cycle power of kites flying crosswind manoeuvres at an elevation angle

β is calculated as follows [16]

$$P_{max} = \frac{4}{27} P_w A \frac{C_L^3}{C_{D,eff}^2} \cos^3 \beta, \quad (12)$$

where $P_w = 1/2\rho V_w^3$ is the wind power density. The ratio $C_L^3/C_{D,eff}^2$ is the non-dimensional force ratio during reel-out where $C_{D,eff} = C_{D,kite} + C_{d,cylinder} l_{tether,avg} d_{tether} / (4A_{kite})$. During the traction phase, a high tether force is desired and thus high lift conditions. However, manoeuvre losses and inertia effects are not taken into account and the tether drag is approximated which will result in a lower achievable cycle power. The wind speed at flight altitude is estimated to be approximately 22 m s^{-1} on average and the elevation angle 30° . It can be expected that the actual power is substantially lower than this theoretical limit of 8.2 MW. With an average power of 3.1 MW the system shows potential of reaching the megawatt-scale with a wing of this size.

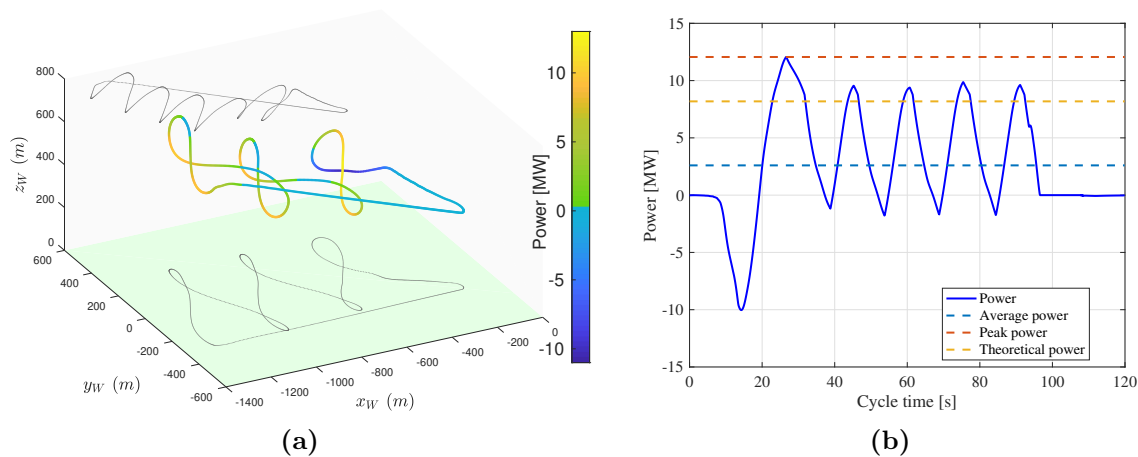


Figure 6. (a) Actual flight path and projections onto the $x_w z_w$ - and $x_w y_w$ -plane with the instantaneous mechanical power production. (b) Detailed power versus cycle time, both simulated at 12 m s^{-1} ground wind speed.

In Figure 7, the force acting on the tether and the speed at which the tether length is extended and contracted are presented. The peak tether force is equal to 617 kN, which is only 37% of the maximum tether force determined by the buckling analysis in [6]. This might be caused by the limitations of using only a small set of parameter to optimise instead of the full system. Also the aggressiveness of the winch is penalised, which might limit the optimiser to use higher tether forces. Undesirably, the force peak reaches almost twice the steady-state value. This requires the tether to be sized for a higher tether force than present during the traction phase. The optimiser makes a trade-off between aggressive winch control and high tether forces. This means the optimiser has not been able to lower the peak with the current objective function. The peak occurs when the sag disappears and the tether straightens out. This introduces high forces on the tether which result in a large overshoot compared to the steady-state. The reel-out and reel-in speeds run into saturation limits at certain positions during the power cycle. This might limit the performance of the aircraft during the power cycle. However, a detailed study of the physical behaviour of the winch and its limits on large-scale systems, is not considered in this work and therefore these limits were not changed from previous studies on small-scale aircraft. It can be seen that the reeling behaviour follows the tether force oscillations but with delay and therefore the tether force keeps oscillating around a steady state value.

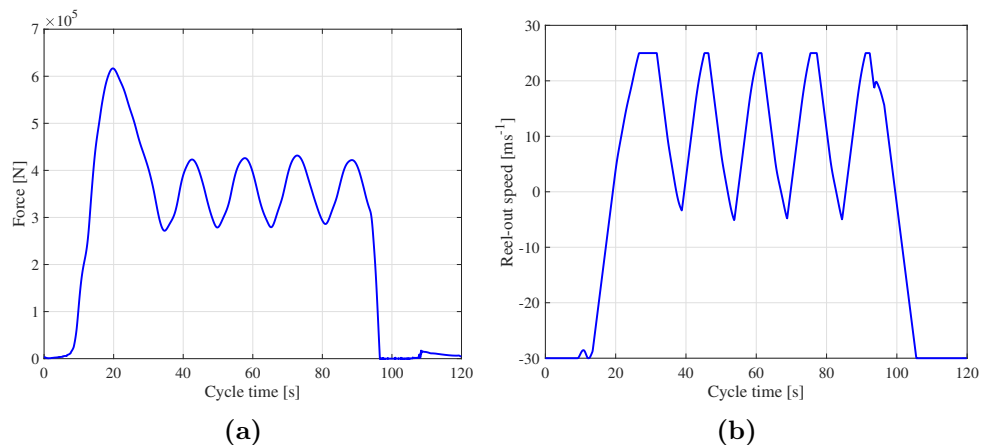


Figure 7. (a) Tether force over a complete pumping cycle. (b) Reel-out speed over a complete pumping cycle, both simulated at 12 m s^{-1} ground wind speed.

A sensitivity analysis of the tether diameter on average cycle power is shown in Figure 8. When the tether diameter increases, the average power output is reduced as expected due to the increase in aerodynamic drag (mass differences are ignored). A linear approximation can then be found relating the tether diameter to the average power output when looking only at the influence of aerodynamic drag.

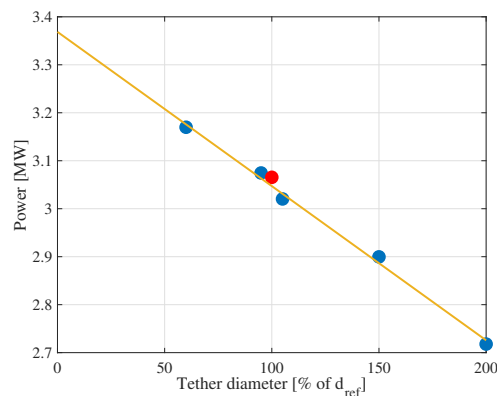


Figure 8. The effect of aerodynamic drag on average cycle power, keeping all variables constant except for tether diameter. The red dot represents a diameter of 0.0297 m. The yellow line is a linear fit of the data points. Simulated at 12 m s^{-1} ground wind speed.

The average mechanical power production over an optimised cycle at different ground wind speeds can be seen in Figure 9. The ground wind speed is the given wind speed at 6m altitude. The optimisations were run at 8, 12, 16, 20 and 22 m s^{-1} . The maximum power output of this system is expected to at around 15 m s^{-1} ground wind speed and equal to 3.8 MW, however there is no certainty as too little wind speeds were optimised up to now. A few extra wind speeds at the lower end have been evaluated using the same controller parameters as coming from the closest optimised wind speed simulation, thus no extra optimisations were performed for these data points. After a specific wind speed the average power output is expected to drop again as can also be seen in Figure 9. In this regime it is expected that the increase in tether drag and the restrained capability of de-powering the aircraft during retraction phase, will limit the power production over a complete cycle. More data points should provide more information

on this phenomenon in the future.

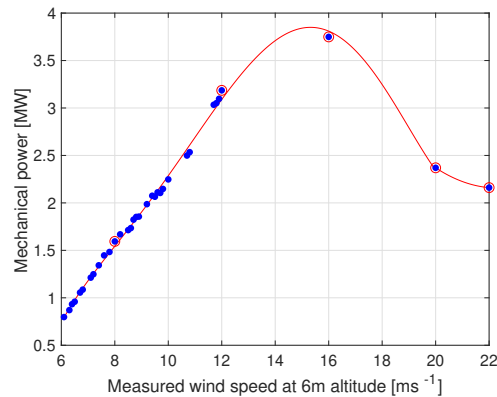


Figure 9. Power curve of the reference system: optimal average mechanical power as a function of average ground wind speed at 6 m altitude. Optimised data points are circled in red.

8. Conclusion and outlook

This work shows the design of a multi-megawatt airborne wind energy reference system. An optimisation framework and full dynamic system simulation is presented as a method to evaluate system performance and optimise flight path- and other controller parameters.

The current results show the potential of a 150 m² wing which is already able to generate multiple megawatts of power. However, the maximum allowable tether force is not reached yet during optimisations. Increasing the number of parameters to optimise, should point out whether the simulation framework is capable of reaching higher tether forces and consecutively producing more power with this aircraft.

Future work will examine the behaviour of the system when using a higher fidelity aerodynamic model taking into account the interaction with the structure. This fluid-structure interaction becomes more essential when discarding the point-mass assumption and using a 6DOF aircraft dynamic model.

Other system components should also be considered in future work. The tether and the winch/generator require more detailed analysis to acquire more accurate results. The model and simulation framework will be made available in open access, to be used for benchmarking and cross validation of alternative simulation frameworks developed by the sector.

Acknowledgements

Sebastian Rapp and Roland Schmehl were financially supported by the project AWESCO (H2020-ITN-642682) funded by the European Union's Horizon 2020 research and innovation programme under the Marie Skłodowska-Curie grant agreement No. 642682l. The authors are grateful to Ampyx Power B.V. for providing some basic sizing information about their large-scale prototype AP-4.

References

- [1] J. Bosch, S. Sieberling, and S. Wilhelm. Status update and review of the AP-3 development. In R. Schmehl and O. Tulloch, editors, *Book of Abstracts of the International Airborne Wind Energy Conference (AWEC 2019)*, pages 12–19, Glasgow, UK, 2019.
- [2] R. Chaitanya, M. Tarkian, and C. Jouannet. Model based aircraft control system design and simulation. In *International Congress of the Aeronautical Sciences*, Nice, France, 2010.
- [3] R. Damiani, F.F. Wendt, J.M. Jonkman, and J. Sicard. A vortex step method for nonlinear airfoil polar data as implemented in kiteaerodyn. In *AIAA Scitech 2019 Forum*, San Diego, CA, 2019.

- [4] M. Diehl, R. Leuthold, and R. Schmehl, editors. *The International Airborne Wind Energy Conference 2017: Book of Abstracts*. University of Freiburg — Delft University of Technology, Freiburg, Germany, 2017.
- [5] S. Drenth. Limiting wave conditions for landing airborne wind energy aircraft on a floating platform. In M. Diehl, R. Leuthold, and R. Schmehl, editors, *Book of Abstracts of the International Airborne Wind Energy Conference (AWEC 2017)*, pages 172–173, Freiburg, Germany, 2017.
- [6] D. Eijkelhof. Design and optimisation framework of a multi-MW airborne wind energy reference system. Master's thesis, Delft University of Technology & Technical University of Denmark, 2019.
- [7] U. Fasel, D. Keidel, G. Molinari, and P. Ermanni. Aeroservoelastic optimization of morphing airborne wind energy wings. In *AIAA Scitech 2019 Forum*, page 1217, San Diego, CA, 2019.
- [8] U. Fasel, P. Tiso, D. Keidel, G. Molinari, and P. Ermanni. Reduced-order dynamic model of a morphing airborne wind energy aircraft. *AIAA Journal*, 57(8):3586–3598, 2019.
- [9] K. Hussen et al. Study on challenges in the commercialisation of airborne wind energy systems. Technical Report PP-05081-2016, prepared for the European Commission's DG Research and Innovation, Ecorys BV, Brussels, September 2018.
- [10] P. Jamieson. *Innovation in Wind Turbine Design*. John Wiley & Sons, Hoboken, NJ, 2 edition, 2018.
- [11] J. Jonkman, S. Butterfield, W. Musial, and G. Scott. Definition of a 5-MW reference wind turbine for offshore system development. Technical report no. NREL/TP-500-38060, National Renewable Energy Laboratory, Golden, CO, February 2009.
- [12] M. Kruijff and R. Ruiterkamp. AP-3, a safety and autonomy demonstrator for utility-scale airborne wind energy. In M. Diehl, R. Leuthold, and R. Schmehl, editors, *Book of Abstracts of the International Airborne Wind Energy Conference (AWEC 2017)*, pages 16–19, Freiburg, Germany, 2017.
- [13] M. Kruijff and R. Ruiterkamp. A roadmap towards airborne wind energy in the utility sector. In *Airborne Wind Energy – Advances in Technology Development and Research*, Green Energy and Technology, pages 643–662. Springer, Singapore, 2018.
- [14] G. Licitra. *Identification and optimization of an airborne wind energy system*. PhD thesis, University of Freiburg, 2018.
- [15] G. Licitra, J. Koenemann, G. Horn, P. Williams, R. Ruiterkamp, and M. Diehl. Viability assessment of a rigid wing airborne wind energy pumping system. In *2017 21st International Conference on Process Control (PC)*, pages 452–458, 2017.
- [16] R.H Luchsinger. Pumping cycle kite power. In U. Ahrens, M. Diehl, and R. Schmehl, editors, *Airborne Wind Energy*, pages 47–64. Springer, Heidelberg Berlin, 2013.
- [17] E.C. Malz, J. Koenemann, S. Sieberling, and S. Gros. A reference model for airborne wind energy systems for optimization and control. *Renewable energy*, 140:1004–1011, 2019.
- [18] J.A. Mehr, E.J Alvarez, and A. Ning. Unsteady aerodynamic analysis of wind harvesting aircraft. In *AIAA Aviation 2020 Forum*, 2020.
- [19] D.J. Moorhouse and R.J. Woodcock. US military specification MIL-F-8785C. *US Department of Defense*, 1980.
- [20] V. Nelson. *Innovative Wind Turbines: An Illustrated Guidebook*. CRC Press, Boca Raton, FL, 2019.
- [21] S. Rapp, R. Schmehl, E. Oland, and T. Haas. Cascaded pumping cycle control for rigid wing airborne wind energy systems. *Journal of Guidance, Control, and Dynamics*, 42(11):2456–2473, 2019.
- [22] R. Schmehl and O. Tulloch, editors. *The International Airborne Wind Energy Conference 2019: Book of Abstracts*. University of Strathclyde — Delft University of Technology, Glasgow, United Kingdom, 2019.
- [23] K. Vimalakanthan, M. Caboni, J.G Schepers, E. Pechenik, and P. Williams. Aerodynamic analysis of Ampyx's airborne wind energy system. *Journal of Physics: Conference Series*, 1037:062008, 2018.
- [24] P. Weiss. Airborne wind energy prepares for take off. *Engineering*, 2019.
- [25] J. Wijnja, R. Schmehl, R. De Breuker, K. Jensen, and D. Vander Lind. Aeroelastic analysis of a large airborne wind turbine. *Journal of Guidance, Control and Dynamics*, 41(11):2374–2385, 2018.